applied optics

Estimation of atmospheric optical turbulence strength in realistic airborne environments

Matthew Kalensky,[1,*] Mark F. Spencer,[2] Eric J. Jumper,[3] and Stanislav Gordeyev[3]

[1]Integrated Engagement Systems Department, Naval Surface Warfare Center Dahlgren Division, Dahlgren, Dahlgren, Virginia 22448, USA
[2]Air Force Research Laboratory, Directed Energy Directorate, Kirtland Air Force Base, Albuquerque, New Mexico 87117, USA
[3]Aerospace and Mechanical Engineering Department, University of Notre Dame, Notre Dame, Indiana 46556, USA
*Corresponding author: mtkalensky@gmail.com

Received 25 March 2022; revised 24 June 2022; accepted 28 June 2022; posted 30 June 2022; published 15 July 2022

In this paper, atmospheric optical turbulence strength is estimated for realistic airborne environments using a modified phase-variance approach, as well as a modified slope-discrepancy approach. Realistic airborne environments are generated using wave-optics simulations of a plane wave propagating through increasing strengths of homogeneous atmospheric optical turbulence, both with and without aero-optical contamination (from in-flight wavefront sensor data) and additive-measurement noise. In comparison to the modified phase-variance approach, the results show that the modified slope-discrepancy approach more accurately estimates atmospheric optical turbulence strength over a wide range of conditions. Such results are encouraging for realistic airborne environments because they can be scaled to different freestream conditions as long as the boundary layer is considered canonical.

https://doi.org/10.1364/AO.459461

1. INTRODUCTION

The index of refraction structure constant, C_n^2, as well as the Fried coherence diameter, r_0, are measures of atmospheric optical turbulence strength and have been used in earnest since the mid-20th century [1–4]. For ground-based measurements, atmospheric optical turbulence strength depends on many factors such as weather, ground terrain, and diurnal cycle, making the estimation of C_n^2 and r_0 challenging. At higher altitudes, it becomes increasingly difficult for researchers to make measurements due to the complexity of the optical setups in realistic airborne environments. As an example, for applications that involve airborne-mounted laser systems [5], it is desirable not only to quantify the strength of atmospheric optical turbulence but also to understand how the presence of other types of aberrations, such as aero-optical contamination and additive-measurement noise, affect the estimation of C_n^2 and r_0.

The work presented here makes use of wave-optics simulations to demonstrate the effectiveness of two approaches at estimating atmospheric optical turbulence strength in realistic airborne environments. The two approaches are (1) a modified phase-variance approach and (2) a modified slope-discrepancy approach. To create a baseline comparison, these approaches are first used on the continuous phase function reconstructed from a Shack–Hartmann wavefront sensor (SHWFS) model. This model is applied to the simulated pupil-plane data generated from wave-optics simulations of a plane wave propagating through increasing strengths of homogeneous atmospheric optical turbulence (but without the presence of other types of aberrations). For this baseline comparison, the atmospheric optical turbulence strength is known as inputs to the wave-optics simulations; therefore, the estimated C_n^2 and r_0 can be directly compared to these inputs, and both approaches show excellent agreement over a wide range of conditions. This outcome, for all intents and purposes, validates the accuracy of the wave-optics simulations.

To simulate the presence of aero-optical contamination, in-flight SHWFS data are used from the Airborne Aero-Optics Laboratory (AAOL). Note that the AAOL consists of high-speed aircraft that enable wavefront measurements in realistic airborne environments [5–19]. In turn, the continuous phase function reconstructed from the in-flight SHWFS data is added to the overall phase function. This addition represents the effects from the receiver-aircraft boundary layer (BL). Also note that throughout this paper, the BL is considered canonical, such that it can be scaled to different freestream conditions.

To simulate the presence of additive-measurement noise, increasing strengths of Gaussian-phase noise is also added to the overall phase function in the estimated pupil plane. This addition represents the effects from multiple random processes via the central-limit theorem. These random processes include, but are not limited to, aero-mechanical and base-motion disturbances, as well as sensor noise.

Once again, since the atmospheric optical turbulence strength is known as inputs to the wave-optics simulations,

the estimated C_n^2 and r_0 can be directly compared to these inputs, even in the presence of aero-optical contamination and additive-measurement noise. In turn, the results ultimately show that compared to the modified phase-variance approach, the modified slope-discrepancy approach more accurately estimates the atmospheric optical turbulence strength over a wide range of conditions. This outcome, at large, validates the use of the modified slope-discrepancy approach for realistic airborne environments.

In what follows, Section 2 describes the wave-optics simulations, which model a plane wave propagating through increasing strengths of homogeneous atmospheric optical turbulence and least-squares phase reconstruction from a SHWFS model. Section 3 formulates the phase-variance and slope-discrepancy approaches used in this paper for estimating atmospheric optical turbulence strength. Both approaches are modified to account for realistic airborne environments via the scaling of aero-optical distortions from the aircraft BL. The results for this paper are presented in Section 4 with a conclusion in Section 5.

2. WAVE-OPTICS SIMULATIONS

The wave-optics simulations performed in this paper were developed in MATLAB, as outlined in this section. These wave-optics simulations made use of the split-step beam propagation method (BPM) to propagate a plane wave through increasing strengths of homogeneous atmospheric optical turbulence. They also made use of a SHWFS model to reconstruct the phase function from the simulated pupil-plane data.

A. Split-Step Beam Propagation Method

In accordance with the split-step BPM [20–25], the simulated atmosphere was broken up into statistically independent volumes. It was assumed that each volume imposed pseudo-random phase variations via randomly generated phase screens. Given plane wave propagation from one phase screen to the next, these pseudo-random phase variations led to irradiance fluctuations known as scintillation.

Using an approach analogous to Ref. [25], the aforementioned phase screens, $\phi(x, y)$, were generated by filtering Gaussian white noise. In particular, the well-known Kolmogorov power spectrum,

$$\Phi_n(\kappa) = 0.033 C_n^2 \kappa^{-11/3}, \tag{1}$$

was used. In Eq. (1), C_n^2 is again the index of refraction structure constant, and $1/L_0 \ll \kappa \ll 1/\ell_0$, where $\kappa = 2\pi/\ell$ is an angular wavenumber, ℓ is a scale size within the inertial subrange, ℓ_0 is the inner scale of the atmospheric optical turbulence, and L_0 is the outer scale. Recall that with a Kolmogorov power spectrum, $\ell_0 = 0$ and $L_0 = \infty$ [25].

Angular-spectrum propagation was used to propagate a unit-amplitude plane wave from one phase screen to the next. The steps were as follows [22,23]. First, let $\psi(x, y, z_1-)$ represent the plane wave incident on the first phase screen and

$$\psi(x, y, z_1) = \psi(x, y, z_1-) \exp(i\phi(x, y)) \tag{2}$$

represent the plane wave leaving the first phase screen.

To simulate propagation, a 2D Fourier transform was used to convert $\psi(x, y, z_1)$ to $\Psi(\kappa_x, \kappa_y, z_1)$. In the spectral domain, $\Psi(\kappa_x, \kappa_y, z_1)$ was multiplied by the free-space transfer function to propagate from the first phase screen to the second phase screen. Next, a 2D inverse Fourier transform was used to convert $\Psi(\kappa_x, \kappa_y, z_2-)$ to $\psi(x, y, z_2-)$. This procedure was repeated for a total of three phase screens. After propagation to the final phase screen, an aperture transmittance function of diameter D was applied to create the simulated pupil-plane data.

In accordance with the split-step BPM, it was assumed that the scintillation was negligible from one phase screen to the next. This assumption was valid since the normalized irradiance variance, $\sigma_I^2 = \langle I^2 \rangle / \langle I \rangle^2 - 1$, was less than 0.1 between the simulated phase screens [22]. Here, $\langle \circ \rangle$ denotes a spatial-average operator, and I is the irradiance. To ensure that aliasing did not affect the results, super Gaussian absorbing boundaries were also incorporated into the wave-optics simulations [25].

B. Shack–Hartmann Wavefront Sensor Model

The simulated pupil-plane data were applied to a SHWFS model. This model divided the associated complex optical fields into subapertures of width d. A thin-lens transmittance function with focal length, f, was then applied to each subaperture, and angular spectrum propagation was used to obtain an irradiance pattern at focus. The centroid was calculated for each irradiance pattern, which provided the x and y slopes for each subaperture. Using least-squares phase reconstruction [5], specifically in a Southwell geometry [26], the measured slopes were reconstructed into a continuous phase function, as shown in Fig. 1.

3. ESTIMATION APPROACHES

In this section, two approaches are formulated to estimate atmospheric optical turbulence strength. Both approaches (i.e., the phase-variance approach and slope-discrepancy approach) are modified to account for the presence of other types of aberrations. These modifications are motivated by the fact that in realistic airborne environments, the continuous phase function reconstructed from wavefront sensor data contains aero-optical contamination. Here, it is assumed that the aero-optical contamination is from the receiver-aircraft BL. It is also assumed that such pupil-plane aberrations are in addition to the distributed-volume aberrations caused by atmospheric optical turbulence.

A. Modified Phase-Variance Approach

The phase variance, in general, scales as $r_0^{-5/3}$ [27]. As such, the tilt-removed phase variance, $\sigma_{\phi_{\mathrm{HO}}}^2$, can be used to estimate atmospheric optical turbulence strength [28], since

$$\sigma_{\phi_{\mathrm{HO}}}^2 = 0.134 \left(\frac{D}{r_0}\right)^{5/3}. \tag{3}$$

Here, subscript HO is used to indicate higher-order aberrations. Assuming conditions with homogeneous atmospheric optical turbulence (i.e., constant C_n^2),

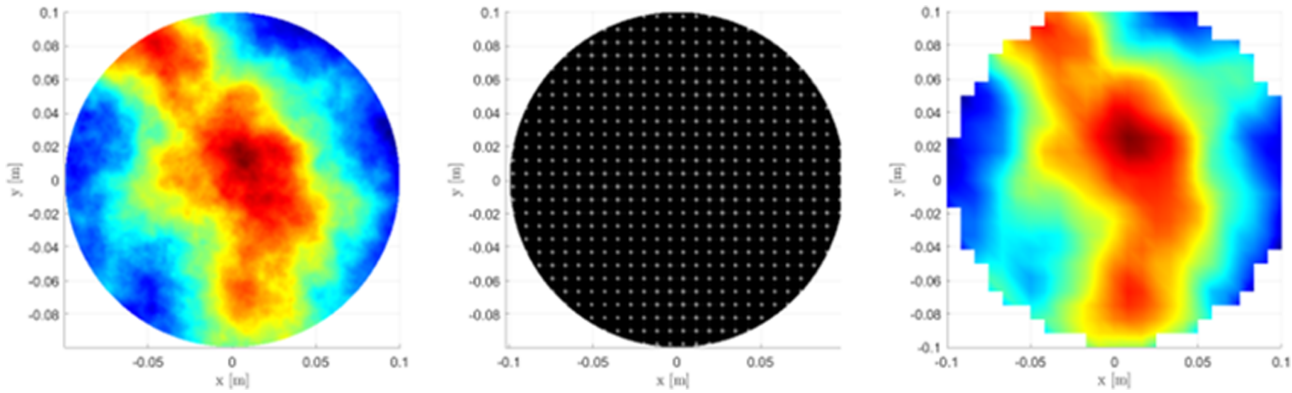

Fig. 1. Examples of simulated pupil-plane phase data from split-step BPM (left), irradiance patterns at focus from the SHWFS model (middle), and continuous phase function reconstructed from the Southwell geometry (right).

$$r_0 = 1.68(C_n^2 Z k^2)^{-3/5} \tag{4}$$

for a plane wave. In Eq. (4), Z is the propagation distance, $k = 2\pi/\lambda$ is an angular wavenumber, and λ is the wavelength. Rearranging Eqs. (3) and (4) results in the following expressions:

$$r_0 = 0.299 \frac{D}{\left(\sigma_{\phi_{\mathrm{HO}}}^2\right)^{5/3}}, \tag{5}$$

and

$$C_n^2 = \frac{2.37}{Z k^2 r_0^{5/3}}, \tag{6}$$

which enable the estimation of r_0 and C_n^2 from $\sigma_{\phi_{\mathrm{HO}}}^2$.

In realistic airborne environments, the estimation of r_0 and C_n^2 from $\sigma_{\phi_{\mathrm{HO}}}^2$ is affected by the presence of other types of aberrations. If these aberrations are independent of each other, then $\sigma_{\phi_{\mathrm{HO}}}^2$ can be estimated using the following approximation:

$$\sigma_{\phi_{\mathrm{HO}}}^2 \approx \sigma_{\phi_{\mathrm{AE}}}^2 - \sigma_{\phi_{\mathrm{BL}}}^2. \tag{7}$$

Here, subscript AE is used to indicate all of the airborne-environment aberrations, whereas subscript BL is used to indicate BL aberrations (due to aero-optical contamination).

Recall that the relationship between measured phase variance and root-mean-square optical path difference is $\sigma_\phi^2 = (k \cdot \mathrm{OPD}_{\mathrm{RMS}})^2$. Also recall that $\mathrm{OPD}_{\mathrm{RMS}}$ scales with BL aberrations. This last point is discussed in more detail later on in this section, as well as in Ref. [29]. With that said, once $\sigma_{\phi_{\mathrm{AO}}}^2$ is known, $\sigma_{\phi_{\mathrm{HO}}}^2$ can be approximated using Eq. (7), and once $\sigma_{\phi_{\mathrm{HO}}}^2$ is approximately known, r_0 and C_n^2 can be estimated using Eqs. (5) and (6), respectively.

B. Modified Slope-Discrepancy Approach

First discovered in the 1980s [30], slope discrepancy is a consequence of using least-squares phase reconstruction to convert measured slopes into a continuous phase function. Tyler showed that the gradient field comprises two components: the gradient of the scalar potential and the curl of the vector potential [31]. It is known that the scalar potential is the component of the continuous phase function reconstructed using least-squares phase reconstruction. Therefore, there is a component of the phase function not accounted for when using least-squares phase reconstruction. This other component of the reconstructed phase function, mathematically referred to as the curl of the vector potential [31], is referred to as slope discrepancy, δ.

Following the analysis of Brennan [32], let θ_L be the measured slopes, otherwise referred to as deflection angles or local jitter. A least-squares reconstructor, H, is then used to convert the measured slopes, θ_L, into a continuous phase function, φ. In practice, φ is related to the gradient of the reconstructed phase, g, through a linear mapping, Γ, such that

$$g = \Gamma\varphi = \Gamma H\theta_L. \tag{8}$$

The difference between the measured slopes and the gradient of the reconstructed phase can then be written as

$$\delta = \theta_L - \Gamma H\theta_L. \tag{9}$$

For greater detail on this derivation, see Ref. [27].

It is important to account for the physical phenomena that contribute to slope discrepancy, δ. It is known that δ results from subaperture fitting error, η, measurement noise, μ, and discontinuities such as branch points or shock waves. For the purpose of the work presented here, assume that branch points and shock waves are nonexistent. This assumption is valid since in most cases, the Rytov number is sufficiently small (below 0.25), and there is nothing protruding into the freestream flow in front of the receiver aperture. Since branch points and shock waves are assumed to be absent, slope discrepancy can be described as $\delta = \eta + \mu$.

To estimate atmospheric optical turbulence strength [27], the slope-discrepancy structure function, D_{SD}, is used, where

$$D_{\mathrm{SD}}(\tau) = \left\langle |\delta(t+\tau) - \delta(t)|^2 \right\rangle. \tag{10}$$

Here, $\langle \circ \rangle$ denotes an ensemble-average operator. Substituting $\delta = \eta + \mu$ into Eq. (10), and expanding and simplifying negligible components leads to the following result:

$$D_{\mathrm{SD}}(\tau) = D_\eta(\tau) + 2\sigma_\mu^2. \tag{11}$$

In other words, D_{SD} is equal to the fitting error structure function, $D_\eta(\tau)$, plus two times the noise variance, σ_μ^2. The assumptions made in arriving at this result are discussed in Ref.

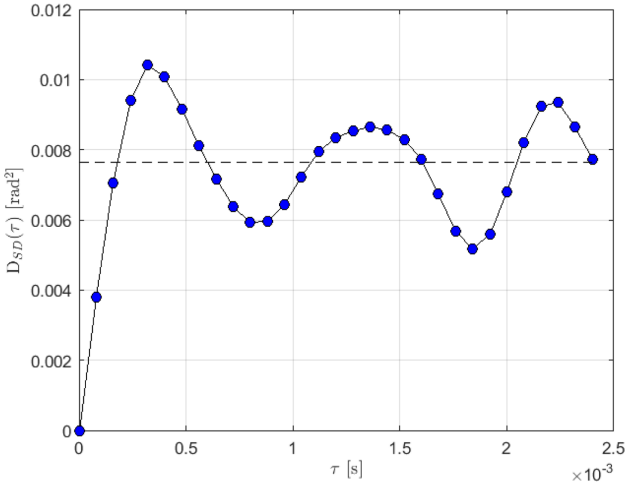

Fig. 2. Example slope-discrepancy structure function. Since the noise variance is removed, the black dashed line represents twice the fitting error variance.

[27] but are also reemphasized later in this section. An example slope-discrepancy structure function with noise removed is presented in Fig. 2.

A relationship between the slope-discrepancy structure function and the fitting error variance is given by

$$\sigma_\eta^2 = \frac{1}{2}(D_{\mathrm{SD}}(\mathcal{T}) - D_{\mathrm{SD}}(0)). \tag{12}$$

Here, $D_{\mathrm{SD}}(0)$ represents twice the noise variance, and $D_{\mathrm{SD}}(\mathcal{T})$ represents the fitting error variance at long time delays, $\mathcal{T}$. In Fig. 2, twice the fitting error variance is represented with the black dashed line (since the noise variance is removed from the slope-discrepancy structure function). This fitting error variance is then related to r_0, *viz.*,

$$\sigma_\eta^2 = \alpha\left(\frac{d}{r_0}\right)^{5/3}, \tag{13}$$

where α is a constant specific to the least-squares phase reconstruction geometry used, and d is again the subaperture width of the SHWFS lenslets. The α constant can be found analytically [33]; however, finding alpha numerically yields a better estimate. This outcome is because the analytical solution does not account for spurious errors such as reconstructed noise. Details on finding α are discussed below after modification to account for the effects of realistic airborne environments.

1. Slope Discrepancy with Aero-optical Contamination Added

It is beneficial to modify the slope-discrepancy approach formulated above to be able to estimate the atmospheric optical turbulence strength in the presence of other types of aberrations, such as aero-optical contamination. In arriving at Eq. (11) from Eq. (10), it was assumed that the slope discrepancy, δ, comprises three components: (1) fitting error, η, (2) measurement noise, μ, and (3) discontinuities such as branch points or shock waves. In realistic airborne environments, the fitting error component contains the distributed-volume aberrations caused by atmospheric optical turbulence in addition to the pupil-plane aberrations caused by the BL.

Assuming that η is the fitting error component that accounts for atmospheric optical turbulence, γ is the fitting error component that accounts for aero-optical contamination, μ is still the measurement-noise component, and branch points and shock waves are absent, the slope discrepancy can be described as $\delta = \eta + \gamma + \mu$.

Substituting $\delta = \eta + \gamma + \mu$ into Eq. (10), the slope-discrepancy structure function, D_{SD}, takes the following form:

$$D_{\mathrm{SD}}(\tau) = \langle |(\eta(t+\tau) + \gamma(t+\tau) + \mu(t+\tau)) - (\eta(t) + \gamma(t) + \mu(t))|^2 \rangle. \tag{14}$$

Upon expansion, the following assumptions are made:

1. $\langle \mu_i \mu_j^T \rangle = \delta_{ij}\sigma_\mu^2 I$,
2. $\langle \mu_i \eta_j^T \rangle = 0I$,
3. $\langle \eta_i \eta_i^T \rangle = \sigma_\eta^2 I$,
4. $\langle \gamma_i \gamma_i^T \rangle = \sigma_\gamma^2 I$,
5. $\langle \mu_i \gamma_j^T \rangle = 0I$,
6. $\langle \eta_i \gamma_j^T \rangle = 0I$.

Here, δ_{ij} is the Kronecker delta, and T represents the transpose operation. Additionally, the subscripts are indexing frame numbers. Assumptions 1 through 3 are defined in Ref. [27] and are used to arrive at Eq. (11). Assumption 1 states that measurement noise is uncorrelated. Assumption 2 states that measurement noise and atmospheric fitting error are uncorrelated. Assumption 3 states that the atmospheric fitting error times itself at the same instant in time reduces to the atmospheric fitting error variance. Assumptions 4 through 6 are novel to this work and have to do with the inclusion of aero-optical contamination. Assumption 4 states that the aero-optical fitting error times itself at the same instant in time reduces to the aero-optical fitting error variance. Assumption 5 states that measurement noise and aero-optical fitting error are uncorrelated. Last, assumption 6 states that the atmospheric and aero-optical fitting errors are independent of each other.

By implementing the aforementioned assumptions, Eq. (14) simplifies, such that

$$D_{\mathrm{SD}}(\tau) = \left\langle \begin{matrix} |\eta(t+\tau)^2 - 2\eta(t+\tau)\eta(t) + \eta(t)^2 + \gamma(t+\tau)^2 \\ -2\gamma(t+\tau)\gamma(t) + \gamma(t)^2 + 2\sigma_\mu^2| \end{matrix} \right\rangle. \tag{15}$$

Notice that the first line of Eq. (15) is just the atmospheric fitting error structure function, $D_\eta(\tau)$, the second line is the aero-optical fitting error structure function, $D_\gamma(\tau)$, and the last line is simply two times the measurement noise variance, σ_μ^2. In turn,

$$D_{\mathrm{SD}}(\tau) = D_\eta(\tau) + D_\gamma(\tau) + 2\sigma_\mu^2, \tag{16}$$

which is an important result. This result indicates that if $D_\gamma(\tau)$ is known, then an estimate of $D_\eta(\tau)$ can be made.

Using Eq. (12), Fig. 2 demonstrates that σ_η^2 can be estimated from $D_{\mathrm{SD}}(\mathcal{T})$. Consequently, rearranging Eq. (12) results in the following relationship:

$$D_{\mathrm{SD}}(\mathcal{T}) = 2\sigma_\eta^2 + 2\sigma_\mu^2. \tag{17}$$

This relationship assumes that slope discrepancy results entirely from atmospheric-induced fitting error and measurement noise. However, as shown in Eq. (16), when aero-optical contamination is also present, an additional fitting error variance term arises. This fitting error contributes to the overall measured slope discrepancy.

At long time delays, Eq. (16) can then be written as

$$D_{\mathrm{SD}}(\mathcal{T}) = 2\sigma_\eta^2 + D_\gamma(\mathcal{T}) + 2\sigma_\mu^2. \tag{18}$$

As a result, r_0 can be solved for using Eqs. (13) and (18), such that

$$r_0 = d\left(\frac{1}{\alpha}\left[\frac{D_{\mathrm{SD}}(\mathcal{T}) - D_\gamma(\mathcal{T}) - 2\sigma_\mu^2}{2}\right]\right)^{-3/5}. \tag{19}$$

Thereafter, C_n^2 can be estimated using Eq. (6).

2. Finding the Alpha Parameter

Equation (13) describes a relationship between the fitting error variance and r_0. In this equation, d is the lenslet subaperture width, and α is a parameter that depends on the geometry of the SHWFS. Reference [33] describes how to analytically derive α; however, as mentioned above, computationally finding α yields better results. As expected, smaller subapertures has less fitting error than larger subapertures. The α parameter accounts for this change in fitting error with varying subaperture size. To find this parameter, wave-optics simulations of known r_0 and constant d were conducted in a Monte Carlo fashion. For each realization, a slope-discrepancy matrix was computed and the variance was calculated. The variance terms were scaled by $(d/r_0)^{5/3}$. The results of this calculation for one simulation realization are presented in Fig. 3.

The mean of these normalized variance terms is the computed α for one simulation iteration. The mean for this simulation iteration is plotted in Fig. 3 as a dashed black line. All resultant α parameters from each simulation iteration were averaged to account for the randomness of the phase screen generation.

C. Scaling the Boundary Layer

To use phase variance or slope discrepancy to estimate the atmospheric optical turbulence strength, it is important to understand how aero-optical contamination (in the form of pupil-plane aberrations from the BL) affects these estimates. As such, the following sections describe how to use the scaling laws for a canonical BL to predict phase variance and slope discrepancy under different freestream conditions. Recall that throughout this paper, the BL is considered canonical, such that it can be scaled to different freestream conditions.

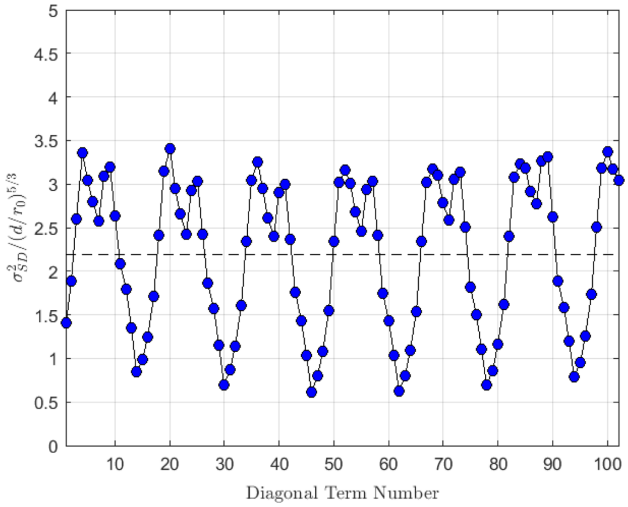

Fig. 3. Normalized variance terms of the slope-discrepancy matrix.

1. Scaling the Boundary Layer to Phase Variance

In recent years, aero-optical BLs have been heavily researched. Many of the major findings are summarized in Ref. [29]. Important scaling laws have been developed that allow the optical distortions associated with canonical BLs to be scaled to different freestream conditions. For subsonic, turbulent BLs, $\mathrm{OPD}_{\mathrm{RMS}}$ scales as

$$\mathrm{OPD}_{\mathrm{RMS}} \approx 0.19 K_{\mathrm{GD}} \rho_\infty M^2 \delta_{\mathrm{BL}} \sqrt{c_f}. \tag{20}$$

Here, K_{GD} is the Gladstone–Dale constant, ρ_∞ is the freestream density, M is the cruise Mach number, δ_{BL} is the BL thickness, and c_f is the skin friction coefficient [29]. The skin friction coefficient, c_f, for incompressible flows can be approximated using the von Kármán–Schoenherr correlation as

$$c_f \approx \frac{1}{17.08(\log \mathrm{Re}_\theta)^2 + 25.11 \log \mathrm{Re}_\theta + 6.012}, \tag{21}$$

where Re_θ is the Reynolds number based on momentum thickness [34]. For a canonical turbulent BL over a flat plate, the BL thickness, δ_{BL}, is approximated as

$$\delta_{\mathrm{BL}} = 0.37 \frac{X}{\mathrm{Re}^{-1/5}}, \tag{22}$$

where X is the streamwise location, and Re is the Reynolds number [35]. For greater detail on the development, assumptions, and limitations of Eq. (20), see Ref. [29]. The scaled $\mathrm{OPD}_{\mathrm{RMS}}$ obtained using Eq. (20) can then be used to estimate $\sigma^2_{\phi_{\mathrm{AO}}}$ in Eq. (7) for wavefront measurements collected at varying altitudes.

2. Scaling Boundary Layer to Slope Discrepancy

As described in Eq. (9), slope discrepancy is the difference between the measured slopes and the gradient of the reconstructed phase. Here, we assume that the measured slopes and the gradient of the reconstructed phase have the same canonical scaling. Since the measured slopes represent the derivative of phase, $\theta_{L_{\mathrm{RMS}}}$ is proportional to $\mathrm{OPD}_{\mathrm{RMS}}$ [given in Eq. (20)] divided by a characteristic length scale [36,37]. For the case of a

turbulent BL, the only relevant length scale is the BL thickness, δ_{BL}. For subsonic flow, the scaling of the measured slopes, θ_L, then becomes

$$\theta_{L_{\mathrm{RMS}}} \sim K_{\mathrm{GD}} \rho_\infty M^2 \sqrt{c_f}. \tag{23}$$

Equation (23) can then be used to scale the gradient of the reconstructed phase time series to different freestream conditions. The scaled time series can then be used to calculate a slope discrepancy structure function associated with the aero-optical BL.

4. RESULTS AND DISCUSSION

The purpose of this section is to assess the accuracy of the two approaches formulated in Section 3 at estimating atmospheric optical turbulence strength over a wide range of conditions. For this purpose, baseline results are first presented, followed by results with both aero-optical contamination and additive-measurement noise added. All of these results make use of the wave-optics simulations outlined in Section 2. Recall that these simulations model a plane wave propagating through increasing strengths of homogeneous atmospheric optical turbulence and least-squares phase reconstruction from a SHWFS model. Also recall that the atmospheric optical turbulence strength is known as inputs to the wave-optics simulations; therefore, the estimated C_n^2 and r_0 can be directly compared to these inputs. With this last point in mind, the results ultimately show that compared to the modified phase-variance approach, the modified slope-discrepancy approach more accurately estimates the atmospheric optical turbulence strength over a wide range of conditions.

A. Baseline Results

To create the baseline results, the aforementioned wave-optics simulations made use of the split-step BPM with $z = 1$ [km] of propagation distance in between three equally spaced phase screens, for a total propagation distance of 3 [km]. An aperture diameter of 0.2 [m] and laser wavelength of 532 [nm] were also used. Assuming Taylor's frozen flow, a stream-wise convective velocity of 165 [m/s] was added to each phase screen and sampled at 12.5 [kHz]. Different optical turbulence strengths were simulated ranging from C_n^2 values of 5×10^{-17} to 5×10^{-15} [$\mathrm{m}^{-2/3}$]. Ten simulation iterations were performed for each turbulence strength. For these simulations, a grid resolution, N, of 1064 and a grid side length, S, of 0.75 [m] were used. The split-step BPM ultimately generated simulated pupil-plane data of a plane wave propagating through increasing strengths of homogeneous atmospheric optical turbulence, and these data were fed into a SHWFS model. For the SHWFS model, a lenslet subaperture width, d, of 1.2 [cm] and a lenslet focal length, f, of 25 [m] were used. The Southwell geometry was also used to perform least-squares phase reconstruction (cf. Fig. 1). Two approaches were then used on the continuous phase function reconstructed from the SHWFS model to estimate atmospheric turbulence strength.

The left plot of Fig. 4 presents the baseline results (average from 10 simulation iterations) for estimating r_0 values using the tilt-removed, phase-variance approach [cf. Eq. (5)]. The x axis represents the input or known r_0 values, and the y axis represents the estimated or measured r_0 values. The linear black line in the plot represents where the measured r_0 values equal the known r_0 values. In the absence of aero-optical contamination and additive-measurement noise, the tilt-removed, phase-variance approach is effective at estimating r_0.

The right plot of Fig. 4 presents the baseline results (average from 10 simulation iterations) for estimating C_n^2 values using the tilt-removed, phase-variance approach [cf. Eq. (6)]. The deviation of the measured C_n^2 values from the known values at stronger atmospheric optical turbulence strengths is associated with appreciable scintillation, which begins to appear in the wave-optics simulation for $C_n^2 > 2 \times 10^{-15}$ [$\mathrm{m}^{-2/3}$].

The results of estimating r_0 using the slope-discrepancy method [cf. Eq. (19)] are presented in the left plot of Fig. 5. The slope discrepancy approach also yields a good estimate

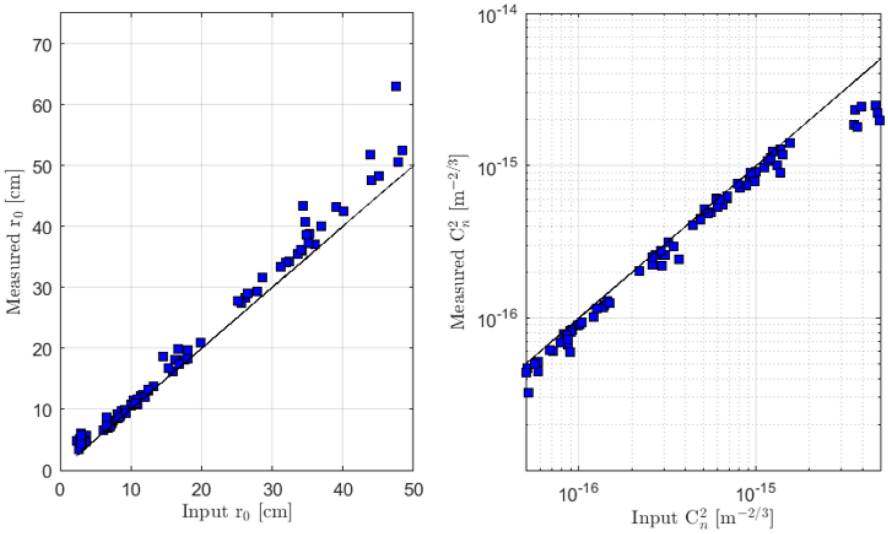

Fig. 4. Baseline results using the phase-variance approach for estimated r_0 values (left) and estimated C_n^2 values (right). The black line denotes where the estimated or measured values equal the input or known values.

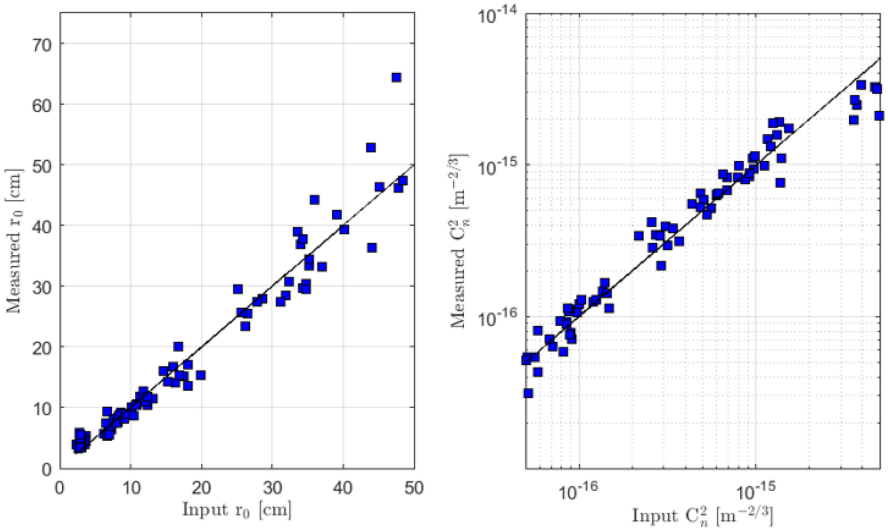

Fig. 5. Baseline results using the slope-discrepancy approach for estimated r_0 values (left) and estimated C_n^2 values (right). The black line denotes where the estimated or measured values equal the input or known values.

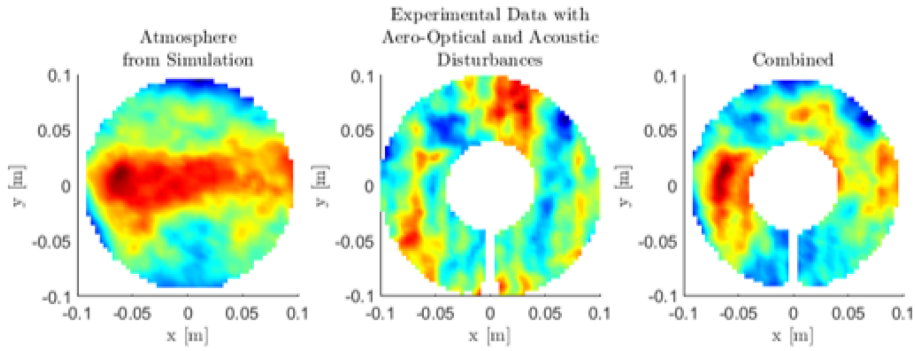

Fig. 6. Comparison of a simulated frame from wave-optics simulations (left), experimental frame from the BL campaign (middle), and overall frame after addition (right).

of r_0. Again, the right plot of Fig. 5 presents the C_n^2 values corresponding to the known and measured r_0 values [cf. Eq. (6)].

For all intents and purposes, the overall agreement found in Figs. 4 and 5 validates the accuracy of the wave-optics simulations. This outcome enables the addition of aero-optical contamination, as well as additive-measurement noise. Results for both additions are discussed in what follows.

B. Results with Aero-optical Contamination Added

When collecting in-flight SHWFS data, the aero-optical contamination associated with the BL of the aircraft introduces additional pupil-plane aberrations. To test the effectiveness of the phase-variance and slope-discrepancy approaches at estimating atmospheric optical turbulence strength in realistic airborne environments, the continuous phase function reconstructed from experimental flight campaigns was added to the overall phase function. For these flight campaigns, two Falcon 10 aircraft flew in close formation and at high altitudes. As such, the atmosphere induced negligible effects onto the measured wavefronts. The in-flight SHWFS data were collected from a laser beam (projected from the transmitter aircraft), which was subjected to distortions primarily from the aero-optical BL in proximity of the receiver aircraft. For convenience, these previous studies are referred to here as the "BL campaign." The continuous phase function reconstructed from the wave-optics simulations and BL campaign had different spatial resolutions. Therefore, the output frames from the wave-optics simulations were interpolated to match the spatial resolution of the BL campaign. Additionally, the BL campaign had a sample rate of 25 [kHz], which was much faster than that of the wave-optics simulations. To match the lower sampling rate, the output frames from the BL campaign data were downsampled temporally. Thereafter, an overall phase function was created by adding the simulated and experimental frames together. An example is shown in Fig. 6, where the left frame is the continuous phase function reconstructed from the wave-optics simulation, the middle frame is the continuous phase function reconstructed from the BL campaign, and the right most frame is the combination of the two.

As shown in Fig. 6, the receiver aircraft made use of a Cassegrain style telescope; therefore, the obscuration associated with the secondary mirror is noticeable in the overall frame. Additionally, a post used to turn a portion of the incoming beam towards a tracking camera introduced an additional obscuration

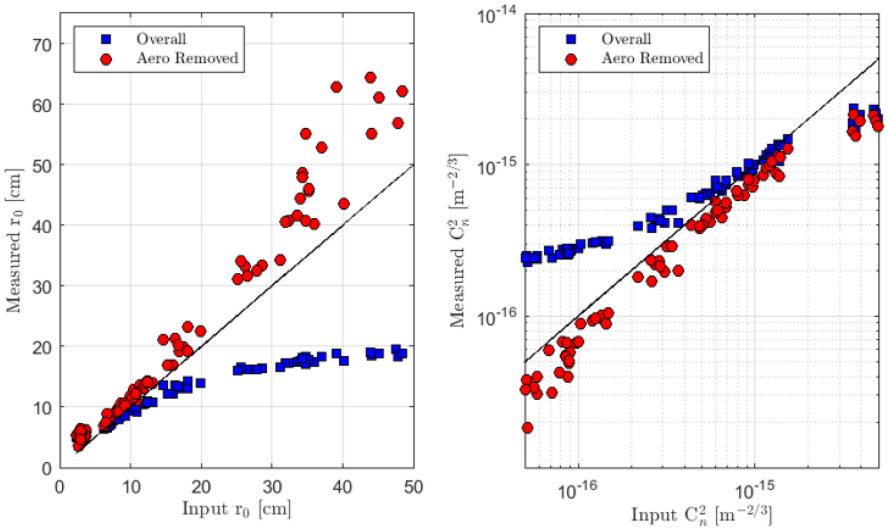

Fig. 7. Results with aero-optical contamination added using the phase-variance approach for estimated r_0 values (left) and estimated C_n^2 values (right). The black line denotes where the estimated or measured values equal the input or known values.

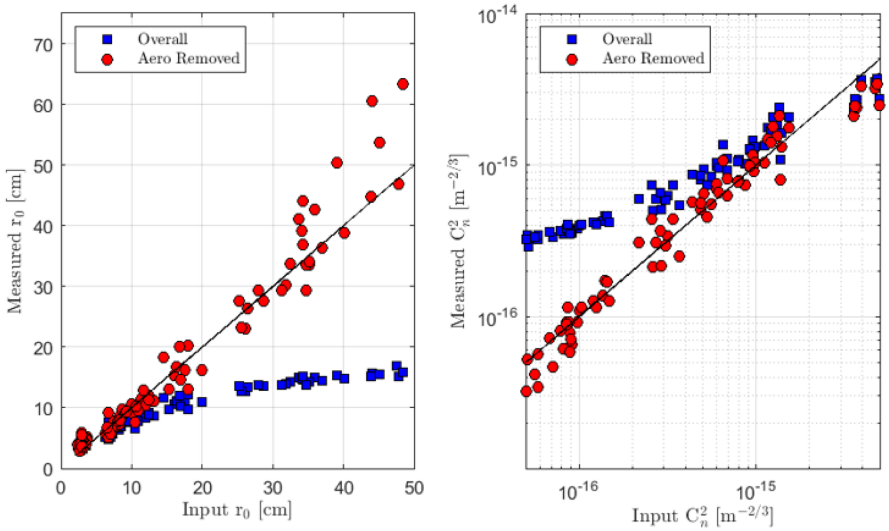

Fig. 8. Results with aero-optical contamination added using the slope-discrepancy approach for estimated r_0 values (left) and estimated C_n^2 values (right). The black line denotes where the estimated or measured values equal the input or known values.

in the bottom of the experimental frames. Since the in-flight SHWFS data were corrupted with mechanical contamination, all tip/tilt was removed before adding experimental frames with the simulated frames.

The left plot of Fig. 7 presents the results of using the phase-variance approach to estimate r_0 when aero-optical contamination is present. Here, the blue squares represent the r_0 estimate when the phase variance of the overall phase function is used. Since the aero-optical disturbances added to the simulated wavefronts introduce additional wavefront error, the overall phase variance is higher and consequently, the estimate of r_0 is poor.

Recall that if the wavefront error associated with the BL is known, it can be removed from the overall phase variance using Eq. (7). The red circles in the left plot of Fig. 7 represent the results when this approach of accounting for the BL is used. Although the estimate is better, r_0 is slightly larger than it should be. Consequently, the resultant C_n^2 values presented in the right plot of Fig. 7 are slightly lower than the known C_n^2 values.

The left plot of Fig. 8 presents the results of using the slope-discrepancy approach to estimate r_0 when aero-optical contamination is present. Here, the blue squares represent the r_0 estimate when the slope discrepancy of the overall phase function is used. As expected, r_0 was predicted to be a much lower value than the known or input r_0 values. The error was larger at lower atmospheric turbulence strengths since the signal to noise ratio between the atmospheric disturbances and the added aero-optical disturbances was smaller.

Section 3.B.1 derived a procedure for decoupling aero-optical and atmospheric related distortions to estimate r_0 using slope discrepancy. Using Eq. (19), r_0 is estimated, and the results

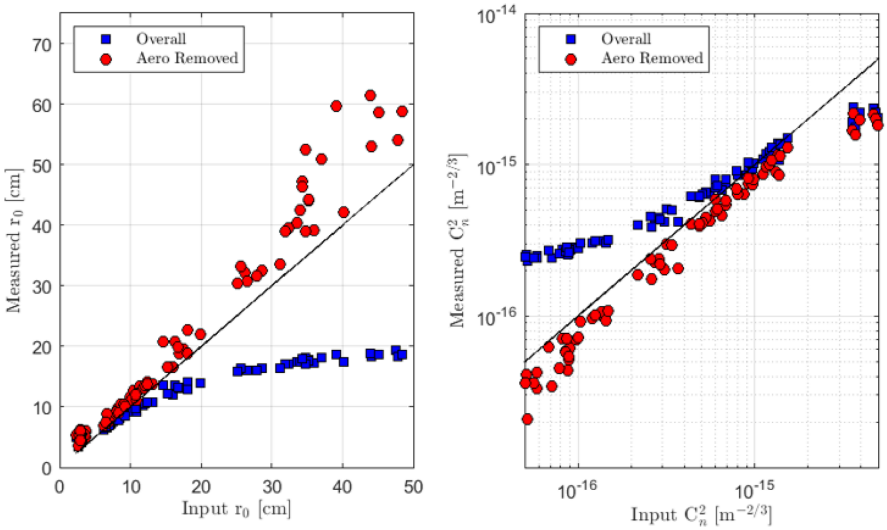

Fig. 9. Results with aero-optical contamination and moderate, additive-measurement noise added using the phase-variance approach for estimated r_0 values (left) and estimated C_n^2 values (right). The black line denotes where the estimated or measured values equal the input or known values.

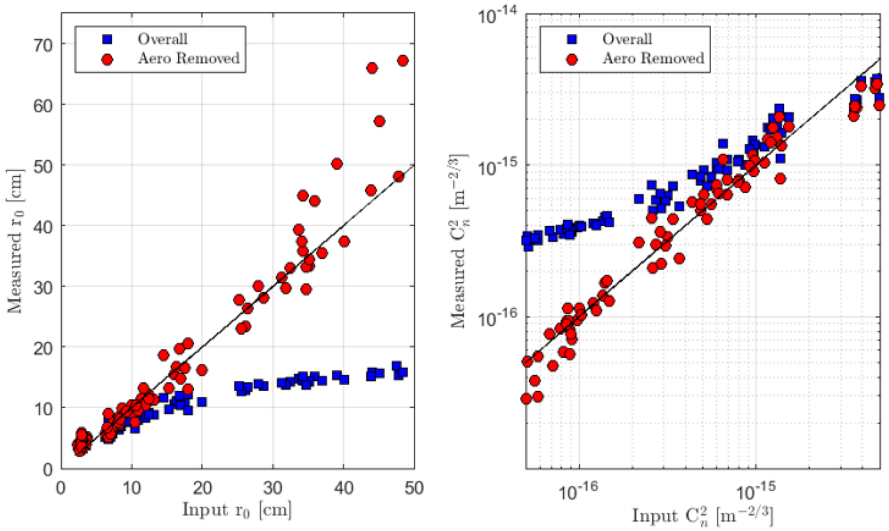

Fig. 10. Results with aero-optical contamination and moderate, additive-measurement noise added using the slope-discrepancy approach for estimated r_0 values (left) and estimated C_n^2 values (right). The black line denotes where the estimated or measured values equal the input or known values.

are presented in the left plot of Fig. 8 as red circles. These r_0 estimates strongly agree with the known r_0 values. The resultant estimates of C_n^2 are presented in the right plot of Fig. 8. Even when aero-optical contamination is present, the modified slope discrepancy approach is effective at estimating atmospheric optical turbulence strength.

C. Simulations with Additive-Measurement Noise Added

This section discusses the effectiveness of the phase-variance and slope-discrepancy approaches for estimating atmospheric optical turbulence strength when additive-measurement noise is present. This noise is in addition to the aero-optical contamination explored in the previous section. Thus, in addition to adding aero-optical contamination from the BL campaign, white-Gaussian noise is also added to the overall phase function.

In what follows, the results present two cases. The first case is simply referred to as the moderate-noise case, and the second case is simply referred to as the severe-noise case. For both cases, the standard deviation of the additive noise is set to be 10% and 50% of the standard deviation of the overall phase function, respectively.

The left plot of Fig. 9 presents the moderate-noise results from using the phase-variance approach to estimate r_0. Again, the blue squares represent the overall phase variance, and the red circles represent the r_0 estimate corresponding to when the BL phase variance is removed. The inclusion of moderate, additive-measurement noise did not appreciably change the results compared to when just aero-optical contamination is included in the overall phase function.

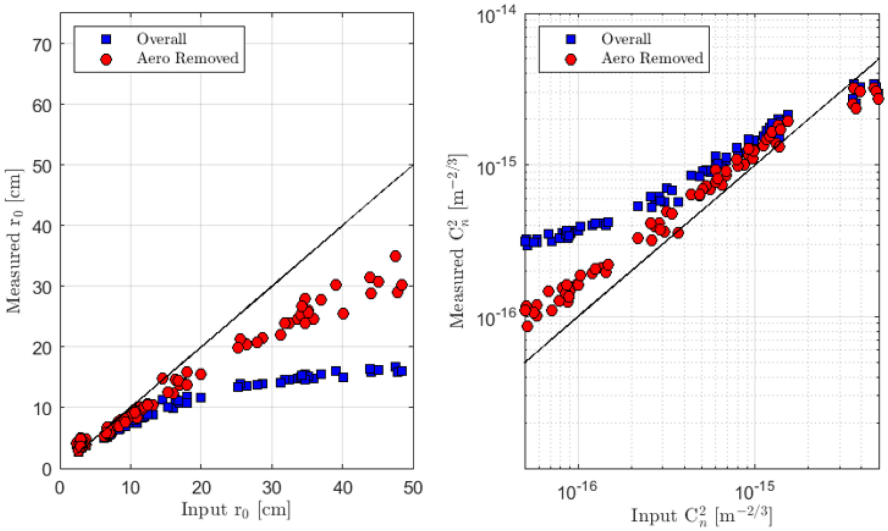

Fig. 11. Results with aero-optical contamination and severe, additive-measurement noise added using the phase-variance approach for estimated r_0 values (left) and estimated C_n^2 values (right). The black line denotes where the estimated or measured values equal the input or known values.

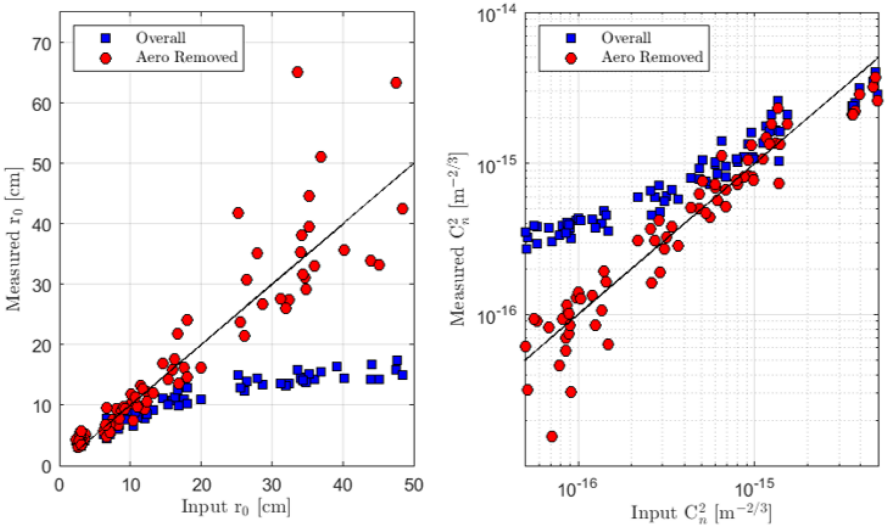

Fig. 12. Results with aero-optical contamination and severe, additive-measurement noise added using the slope-discrepancy approach for estimated r_0 values (left) and estimated C_n^2 values (right). The black line denotes where the estimated or measured values equal the input or known values.

The moderate-noise results using the slope-discrepancy approach are presented in Fig. 10. Similar to the phase-variance approach, the inclusion of moderate, additive-measurement noise did not appreciably affect the r_0 and C_n^2 estimates.

The severe-noise results using the phase-variance approach are presented in Fig. 11. Here, it can be seen that even with the aero-optical contamination removed, the inclusion of severe, additive-measurement noise causes the phase-variance approach to overestimate the atmospheric optical turbulence strength. In other words, the r_0 values are lower than expected, and the C_n^2 values are higher than expected.

The severe-noise results using the slope-discrepancy approach are presented in Fig. 12. As described in Section 3.B, this method is more noise resistant. As can be seen, even with the inclusion of severe, additive-measurement noise, the slope-discrepancy approach still yields reasonable estimates of r_0 compared to the known value. The resultant C_n^2 values are shown in the right plot of Fig. 12.

These results are extremely encouraging. For realistic airborne environments, slope discrepancy, coupled with the approach derived in Section 3.B.1, provides a high-fidelity approach for estimating the atmospheric optical turbulence strength even when aero-optical contamination and additive-measurement noise are present in the measured wavefronts. As long as the BL is considered canonical, the measured slopes and the gradients of reconstructed phase can be scaled to different freestream conditions using the methods described in Section 3.C.

D. Summary of Results

The error associated with estimating r_0 is summarized in Table 1. Here, the error is calculated as

Table 1. Error Summary

Simulation Type	PV	PV w/o Aero	SD	SD w/o Aero
Atm. only	20.62%	N/A	18.10%	N/A
Atm. w/aero	36.48%	34.80%	38.88%	18.92%
Atm. w/aero + 10% additive noise	36.42%	31.80%	38.77%	19.12%
Atm. w/aero + 50% additive noise	38.07%	24.03%	38.80%	30.32%

$$\text{ERROR} = \left\langle \frac{|r_{0_{\text{MEASURED}}} - r_{0_{\text{ACTUAL}}}|}{r_{0_{\text{ACTUAL}}}} \times 100 \right\rangle, \tag{24}$$

where the brackets indicate ensemble averaging.

In Table 1, it can be seen that when only atmospheric optical turbulence is present, both the phase-variance and slope-discrepancy approaches yield reasonable estimates of r_0 with errors of 20.6% and 18.1%, respectively.

When aero-optical contamination is added, it can be seen that both approaches yield poor estimates. Recall that the modified phase-variance (PV w/o aero in Table 1) approach and the modified slope-discrepancy (SD w/o aero in Table 1) approach were employed as a result. While the modified phase-variance approach only marginally decreases the error, the modified slope-discrepancy approach drastically reduces the error from 38.9% to 18.9%. Since realistic measurement noise is already embedded (cf. Fig. 6), the modified slope-discrepancy approach is extremely effective at estimating atmospheric optical turbulence strength in realistic airborne environments. This claim is substantiated by both the error given in Table 1 and the results presented in Fig. 8.

Table 1 also presents the error for two cases with additive-measurement noise added. For the moderate-noise case (10% additive noise), the modified phase-variance approach still yields poor estimates of r_0, while the modified slope-discrepancy approach remains effective with an error of only 19.1%. As the measurement noise is raised unrealistically high, as for the severe-noise case (50% additive noise), it can be seen that both the modified phase-variance and slope-discrepancy approaches return poor estimates of r_0. However, it should be noted that although the error using the modified slope-discrepancy approach increases, the estimate trends remain reasonable, which is reflected in Fig. 12, the same of which cannot be said for the modified phase-variance approach in Fig. 11.

5. CONCLUSION

In this paper, atmospheric optical turbulence strength was estimated for realistic airborne environments using modified phase-variance and slope-discrepancy approaches. The realistic airborne environments were generated using wave-optics simulations of a plane wave propagating through increasing strengths of homogeneous atmospheric optical turbulence, both with and without aero-optical contamination (from in-flight wavefront sensor data), as well as additive-measurement noise. In turn, the results showed that compared to the modified phase-variance approach, the modified slope-discrepancy approach more accurately estimated the atmospheric optical turbulence strength over a wide range of conditions. These results are encouraging for realistic airborne environments because they can be scaled to different freestream conditions as long as the BL is considered canonical.

Funding. Office of Naval Research (N00014-18-1-2112); Directed Energy Joint Transition Office (FA9550-13-1-0001).

Acknowledgment. The authors thank the Directed Energy Joint Transition Office and Office of Naval Research for sponsoring this research, as well as T. J. Brennan and M. R. Kemnetz for many insightful discussions regarding the results presented within. This work is approved for public release; distribution is unlimited. Public Affairs release approval # NSWCDD-PN-22-00052.

Disclosures. The authors declare no conflicts of interest.

Data availability. Data underlying the results presented in this paper are not publicly available at this time but may be obtained from the authors upon reasonable request.

REFERENCES

1. D. L. Fried, "Statistics of a geometric representation of wavefront distortion," J. Opt. Soc. Am. **55**, 1427–1435 (1965).
2. D. L. Fried, "Limiting resolution looking down through the atmosphere," J. Opt. Soc. Am. **56**, 1380–1384 (1966).
3. D. L. Fried, "Optical resolution through a randomly inhomogeneous medium for very long and very short exposures," J. Opt. Soc. Am. **56**, 1372–1379 (1966).
4. D. Fried, "Optical heterodyne detection of an atmospherically distorted signal wave front," Proc. IEEE **55**, 57–77 (1967).
5. P. H. Merritt and M. F. Spencer, *Beam Control for Laser Systems*, 2nd ed. (Directed Energy Professional Society, 2018).
6. S. Gordeyev and E. Jumper, "Fluid dynamics and aero-optics of turrets," Prog. Aerosp. Sci. **46**, 388–400 (2010).
7. E. J. Jumper, M. Zenk, S. Gordeyev, D. Cavalieri, and M. R. Whiteley, "The airborne aero-optics laboratory, AAOL," Proc. SPIE **8395**, 839507 (2012).
8. N. De Lucca, S. Gordeyev, and E. Jumper, "The airborne aero-optics laboratory, recent data," Proc. SPIE **8395**, 839508 (2012).
9. T. J. Brennan and D. J. Wittich, "Statistical analysis of airborne aero-optical laboratory optical wavefront measurements," Opt. Eng. **52**, 071416 (2013).
10. C. Porter, S. Gordeyev, M. Zenk, and E. Jumper, "Flight measurements of the aero-optical environment around a flat-windowed turret," AIAA J. **51**, 1394–1403 (2013).
11. M. J. Krizo, S. J. Cusumano, S. T. Fiorino, R. Heap, V. Velten, J. Brown, and R. J. Bartell, "Design, development, and in-flight testing of a pointer/tracker for in-flight experiments to measure aero-optical effects over a scaled turret," Opt. Eng. **52**, 071415 (2013).
12. M. Kalensky, S. Gordeyev, and E. J. Jumper, "In-flight studies of aero-optical distortions around AAOL-BC," in *Aviation Forum* (American Institute of Aeronautics and Astronautics, 2019).
13. M. Kalensky, J. Wells, E. J. Jumper, and S. Gordeyev, "Image degradation due to various aero-optical environments," Proc. SPIE **11102**, 111020F (2019).
14. M. Kalensky, E. Jumper, M. Whiteley, Y. Diskin, S. Gordeyev, R. Drye, A. Archibald, and M. Grose, "Turbulence profiling using AAOL-BC," in *SciTech Forum* (American Institute of Aeronautics and Astronautics, 2020).
15. S. Gordeyev and M. Kalensky, "Effects of engine acoustic waves on aerooptical environment in subsonic flight," AIAA J. **58**, 5306–5317 (2020).
16. M. Kalensky, J. Wells, and S. Gordeyev, "Image degradation due to different in-flight aero-optical environments," Opt. Eng. **59**, 104104 (2020).
17. Y. Diskin, M. Whiteley, M. Grose, K. Jackovitz, R. Drye, B. Hampshire, M. Owens, E. Smith, E. Magee, M. Kalensky, E. Jumper, S. Gordeyev, and A. Archibald, "Aircraft to ground profiling: turbulence measurements and optical system performance modeling," AIAA J. **59**, 4610–4625 (2021).

18. M. Kalensky, E. J. Jumper, M. R. Kemnetz, and S. Gordeyev, "In-flight measurement of atmospheric-imposed tilt: experimental results and analysis," Appl. Opt. **61**, 4874–4882 (2022).
19. M. Kalensky, "Airborne measurement of atmospheric-induced beam jitter," Ph.D. thesis (University of Notre Dame, 2022).
20. D. Knepp, "Multiple phase-screen calculation of the temporal behavior of stochastic waves," Proc. IEEE **71**, 722–737 (1983).
21. C. MaCaskill and T. E. Ewart, "Computer simulation of two-dimensional random wave propagation," IMA J. Appl. Math. **33**, 1–15 (1984).
22. J. M. Martin and S. M. Flatté, "Intensity images and statistics from numerical simulation of wave propagation in 3-D random media," Appl. Opt. **27**, 2111–2126 (1988).
23. J. M. Martin and S. M. Flatté, "Simulation of point-source scintillation through three-dimensional random media," J. Opt. Soc. Am. **7**, 838–847 (1990).
24. M. C. Roggemann and W. M. Byron, *Imaging Through Turbulence* (CRC Press, 1996).
25. J. Schmidt, *Numerical Simulation of Optical Wave Propagation with Examples in MATLAB* (SPIE, 2010).
26. W. H. Southwell, "Wave-front estimation from wave-front slope measurements," J. Opt. Soc. Am. **70**, 998–1006 (1980).
27. T. J. Brennan and D. C. Mann, "Estimation of optical turbulence characteristics from Shack Hartmann wavefront sensor measurements," Proc. SPIE **7816**, 781602 (2010).
28. R. J. Noll, "Zernike polynomials and atmospheric turbulence," J. Opt. Soc. Am. **66**, 207–211 (1976).
29. S. Gordeyev, A. E. Smith, J. A. Cress, and E. J. Jumper, "Experimental studies of aero-optical properties of subsonic turbulent boundary layers," J. Fluid Mech. **740**, 214–253 (2014).
30. D. M. Winker, G. A. Ameer, S. L. Brown, G. C. Cochran, R. Dueck, D. L. Fried, D. M. Lussier, W. Moretti, P. H. Roberts, K. E. Steinhoff, and G. A. Tyler, "Characteristics of turbulence measured on a large aperture," Proc. SPIE **926**, 360–366 (1988).
31. G. A. Tyler, "Reconstruction and assessment of the least-squares and slope discrepancy components of the phase," J. Opt. Soc. Am. **17**, 1828–1839 (2000).
32. T. J. Brennan, "Anatomy of the slope discrepancy structure function: characterization of turbulence," Proc. SPIE **5087**, 103–114 (2003).
33. J. Vaughn, "The variability of r0 estimates," Technical Report (The Optical Sciences Company, 2002).
34. J. Bardina, P. Huang, and T. Coakley, "Turbulence modeling validation, testing, and development," Technical Report (NASA, 1997).
35. H. Schlichting, *Boundary-layer Theory* (Springer, 2000).
36. M. R. Kemnetz and S. Gordeyev, "Analysis of aero-optical jitter in convective turbulent flows using stitching method," AIAA J. **60**, 14–30 (2021).
37. J. Sontag and S. Gordeyev, "Optical diagnostics of spanwise-uniform flows," AIAA J. 1 (2022).